Reduction of Uranium(VI) by Mixed Iron(II)/Iron(III) Hydroxide (Green Rust): Formation of UO$_2$ Nanoparticles

EDWARD J. O'LOUGHLIN,*,[†]
SHELLY D. KELLY,[†] RUSSELL E. COOK,[‡]
ROSEANN CSENCSITS,[‡] AND
KENNETH M. KEMNER[†]

Environmental Research Division and Materials Science Division, Argonne National Laboratory, Argonne, Illinois 60439-4843

Green rusts, which are mixed ferrous/ferric hydroxides, are found in many suboxic environments and are believed to play a central role in the biogeochemistry of Fe. Analysis by U L$_{III}$-edge X-ray absorption near edge spectroscopy of aqueous green rust suspensions spiked with uranyl (U^{VI}) showed that U^{VI} was readily reduced to U^{IV} by green rust. The extended X-ray absorption fine structure (EXAFS) data for uranium reduced by green rust indicate the formation of a UO$_2$ phase. A theoretical model based on the crystal structure of UO$_2$ was generated by using FEFF7 and fitted to the data for the UO$_2$ standard and the uranium in the green rust samples. The model fits indicate that the number of nearest-neighbor uranium atoms decreases from 12 for the UO$_2$ structure to 5.4 for the uranium-green rust sample. With an assumed four nearneighbor uranium atoms per uranium atom on the surface of UO$_2$, the best-fit value for the average number of uranium atoms indicates UO$_2$ particles with an average diameter of 1.7 ± 0.6 nm. The formation of nanometer-scale particles of UO$_2$, suggested by the modeling of the EXAFS data, was confirmed by high-resolution transmission electron microscopy, which showed discrete particles (~2–9 nm in diameter) of crystalline UO$_2$. Our results clearly indicate that U^{VI} (as soluble uranyl ion) is readily reduced by green rust to U^{IV} in the form of relatively insoluble UO$_2$ nanoparticles, suggesting that the presence of green rusts in the subsurface may have significant effects on the mobility of uranium, particularly under iron-reducing conditions.

Introduction

Many activities associated with the mining, extraction, and processing of uranium for nuclear fuel and weapons as well as the processing of spent fuel have generated substantial quantities of waste materials contaminated with uranium and other radionuclides. In many cases, past practices relating to the handling and storage of such waste materials have resulted in extensive contamination of the subsurface by these elements. Indeed, nearly 70% of U.S. Department of Energy (DOE) facilities report groundwater contamination by radionuclides (*1*). At most sites, subsurface contamination by uranium and other radionuclides is due to the presence of species with potentially high mobility in the subsurface (typically species with high aqueous solubility), which in time results in highly dispersed contaminant plumes. Processes suitable for in situ remediation of radionuclides include permeable reactive barriers, chemical stabilization/immobilization, and biotransformation. For radionuclides such as uranium and technetium, species at the higher oxidation states (e.g., U^{VI} and Tc^{VII}) are generally thought to be more soluble/mobile than more reduced species (e.g., U^{IV} and Tc^{IV}). Thus, the transformation of radionuclides such as uranium and technetium from an oxidized form to a more reduced form is seen as an attractive approach for their immobilization/stabilization in situ.

In the subsurface, radionuclides such as uranium can be reduced by a number of abiotic and microbially mediated processes. Although several bacteria that can directly reduce U^{VI} have been identified (*2–5, among others*), significant reduction of U^{VI} to U^{IV} may also result from interaction of U^{VI} with reductants directly or indirectly formed by the metabolic processes of facultative and strict anaerobes, particularly iron- and sulfate-reducing bacteria. Dissimilatory iron reducing (DIR) bacteria are a diverse group that couples the oxidation of organic compounds or hydrogen to Fe^{III} reduction. The reduction of Fe^{III} by DIR bacteria results in the production of soluble Fe^{II} complexes, sorption of Fe^{II} to organic and inorganic phases, and the formation of a host of Fe^{II}-bearing mineral phases including magnetite, siderite, vivianite, ferruginous smectite, and green rust (*6–10*). The reduction of U^{VI} to U^{IV} by many Fe^{II} species is thermodynamically favorable, and indeed evidence from both field and laboratory studies suggests a link between iron redox cycling and the genesis of certain uranium ore formations (*11, 12*). However, studies of U^{VI} reduction by Fe^{II} species to date have focused primarily on ferrous sulfide (*13*) and Fe^{II} sorbed to Fe^{III} oxyhydroxides (*2, 14, 15*), while the reduction of U^{VI} by other Fe^{II}-bearing phases has been largely unexamined.

Green rusts are layered Fe^{II}-Fe^{III} hydroxides having a pyroaurite-type structure consisting of alternating positively charged hydroxide layers and hydrated anion layers. Isomorphic substitution of Fe^{3+} for Fe^{2+} in the trioctahedral sheets of Fe(OH)$_2$ confers a positive charge to the hydroxide layer that is balanced by hydrated anions in the interlayer (typically Cl$^-$, SO$_4$$^{2-}$, or CO$_3$$^{2-}$). Green rusts are formed by a number of abiotic and biotic processes under circumneutral to alkaline conditions in suboxic environments. They have been identified as products of both abiotic and microbially induced corrosion of iron and steel (*16–19*); indeed, the formation of green rusts in zerovalent iron permeable reactive barriers has been reported by several investigators (*20–23*). In addition, the formation of green rusts by bacteria known to be key players in the biogeochemical cycling of Fe has recently been reported. Various strains of the DIR bacterium *Shewanella putrefaciens* produce green rusts as products of the bioreduction of hydrous ferric oxide and lepidocrocite (*8, 24–27*). Moreover, green rusts are also observed as products of the anaerobic biooxidation of Fe^{II} by *Dechlorosoma suillum* (*28*).

The characteristic bluish green color of hydromorphic soils has long been presumed to be due to the presence of mixed Fe^{II}/Fe^{III} hydroxide species (*29*); however, the unam-

---

* Corresponding author phone: (630)252-9902; fax: (630)252-9793; e-mail: oloughlin@anl.gov. Corresponding author address: Environmental Research Division, Argonne National Laboratory, Building 203, Room E-137, 9700 South Cass Ave., Argonne, IL 60439-4843.
[†] Environmental Research Division.
[‡] Materials Science Division.

biguous identification of green rusts in suboxic soils and sediments has been complicated by the rapid oxidation of these compounds upon exposure to air. Oxidation of green rusts results in the formation of ferrihydrite, goethite (α-FeOOH), akakaneite (β-FeOOH), lepidocrocite (γ-FeOOH), δ-FeOOH, maghemite (γ-Fe$_2$O$_3$), or magnetite (Fe$_3$O$_4$), depending on pH, solution composition, oxidant, rate of oxidation, and the degree and rate of dehydration (30–36). Direct evidence for the presence of green rusts in hydromorphic soils has recently been reported (37, 38), and this material has been tentatively identified as hydroxy-green rust (GR$_{OH}$) (39). Recent work by Bourrié et al. suggests that the solubility of Fe in soil solutions in hydromorphic soils is controlled by equilibrium with GR$_{OH}$ (40). As metastable intermediates in the transformation of Fe^{II} to magnetite and Fe^{III} oxyhydroxides (e.g., lepidocrocite and goethite) at nearly neutral to slightly alkaline pH, green rusts are believed to play a central role in the redox cycling of Fe in aquatic and terrestrial environments.

Recent research has shown that green rusts are capable of reducing a number of organic and inorganic contaminants (30, 41–47), suggesting that green rusts may be highly reactive reductants in suboxic environments. In addition to their ability to reduce many contaminants, green rusts might also affect contaminant fate and transport by sequestration. For example, the reduction of Cr^{VI} by green rust results in the formation of a Cr^{III}-Fe^{III} oxyhydroxide similar to 2-line ferrihydrite (30). In addition, other cations might isomorphically substitute for Fe^{2+} and/or Fe^{3+} during green rust formation. Indeed, isomorphic substitution of Ni^{2+}, Zn^{2+}, Cd^{2+}, Co^{2+}, and Mg^{2+} for Fe^{2+} has been reported (27, 48–50). Moreover, the formation of U^{4+} and Tc^{4+} isomorphically substituted green rust phases has been observed during the electrochemical reduction of U^{VI} and Tc^{VII} in aqueous solutions (51). The incorporation of cationic inorganic contaminants into the structures of green rusts or green rust oxidation products (e.g., magnetite and goethite) could provide an effective means of sequestering contaminants in the subsurface.

The results of these studies suggest that green rusts play an important role in the fate and transport of many contaminants in suboxic soils and sediments. This paper examines the reduction of U^{VI} to U^{IV} by hydroxysulfate green rust, resulting in the formation of UO$_2$ nanoparticles.

Experimental Section

Experimental Setup. Hydroxysulfate green rust (GR$_{SO_4}$), a green rust in which SO$_4^{2-}$ is the interlayer anion, was synthesized by air oxidation of a 1.0 M ferrous sulfate solution. Briefly, 278 g of FeSO$_4$·7H$_2$O (99+%, Aldrich) was dissolved in 1 L of distilled deionized water on a magnetic stirrer under ambient atmosphere. Upon dissolution, the solution was titrated with 1.0 M NaOH until the pH reached 7.5, at which point the GR$_{SO_4}$ suspension was placed in a glovebox. All subsequent sample preparation and experimental setup occurred in an anoxic atmosphere (4–6% H$_2$ in N$_2$). The green rust was recovered by centrifugation and subsequently washed four times with deoxygenated, distilled deionized water. X-ray diffraction (XRD) analysis of the GR$_{SO_4}$ suspension indicated that the final product was free of measurable amounts of other Fe-bearing solid phases (e.g., magnetite, goethite, lepidocrocite).

The reaction system consisted of 50-mL conical polypropylene centrifuge tubes with screw caps. Reactions were initiated by adding 10 mL of 20 mM uranium acetate [UO$_2$(CH$_3$COO)$_2$·2H$_2$O; ≥98%, Fluka] to 35 mL of suspensions containing 2 g of GR$_{SO_4}$. The resulting suspensions had an initial pH of 7.3. After 48 h, the pH of the suspensions was measured, the suspensions were centrifuged, and the supernatant was saved for uranium analysis by inductively

coupled plasma-optical emission spectroscopy (ICP-OES). The uranium-green rust (U-GR) pellets were resuspended in deoxygenated, distilled deionized water, and centrifuged again; the green rust pellets were washed two more times in this manner. After the final washing, subsamples were removed for analysis by X-ray absorption fine structure (XAFS) spectroscopy, XRD, and imaging by transmission electron microscopy (TEM).

X-ray Absorption Spectroscopy. XAFS is an element-specific, short-range structural probe that provides qualitative and quantitative information on the local structural and compositional environment of the absorbing atom (52). Data were collected for both X-ray absorption near edge structure (XANES), an in situ probe that provides information about the oxidation state and coordination geometry of the absorbing atom (53), and extended X-ray absorption fine structure (EXAFS), which provides information on the type and number of the atoms surrounding the absorbing atom as well as the radial distances to those atoms (54).

Fluorescence XAFS measurements were made on wet, homogeneous U-GR pastes mounted in holes machined in Plexiglas sample holders. The holes were covered with Kapton film held in place with Kapton tape. Aqueous solutions of reduced resorufin (a redox indicator dye; solutions of reduced resorufin will turn from colorless to pink upon exposure to molecular oxygen) mounted in this manner and exposed to air remained colorless for more than 8 h, indicating that such sample mounts are effective for excluding oxygen from samples during analysis. The samples were stored in an O$_2$-free atmosphere prior to analysis. XAFS data were collected at the Materials Research Collaborative Access Team (MR-CAT) sector 10-ID beamline at the Advanced Photon Source (APS) at Argonne National Laboratory (55). Data for XANES and EXAFS spectra were collected at the U L$_{III}$-edge. The energy of the incident X-rays was selected by using Bragg reflection from two silicon (111) crystals. X-rays with higher-harmonic energies were rejected by using a rhodium mirror. The incident X-ray intensity was sampled with a nitrogen-filled ion chamber, and the filtered fluorescent X-ray intensity was sampled by using an argon-filled ion chamber detector in the Stern-Heald geometry (56), with a strontium filter of six absorption lengths. Linearity tests (57) indicated less than 0.30% nonlinearity for a 50% decrease in incident X-ray intensity. The incident X-ray intensity varied by less than 15% throughout the energy range of the XAFS measurements. Three scans were collected at six different locations on each sample to reduce radiation exposure and minimize radiation-induced changes in the samples. The sample was exposed to the X-ray beam for approximately 1 min per measurement at each location. Measuring several spectra at different sample locations enabled determination of radiation-induced chemical effects at the 1-min time scale. No time-dependent change in the XAFS data was observed for any of the samples.

The position of the absorption edge (the rise in the adsorption coefficient due to the excitation of core electrons) is directly related to the valence state of uranium. Thus, XANES spectra are particularly sensitive to subtle changes in the calibration of the monochromator, and careful monitoring of the monochromator energy is required. The transmission XAFS signal of an yttrium foil was used as a reference to calibrate the energy positions of the XANES spectra from the uranium standards and U-GR samples, as described by Cross and Frenkel (58).

The codes contained in the UWXAFS package (59) were used to analyze the EXAFS data. The program FEFF7 (60) was used to construct the theoretical model on the basis of the crystallographic atomic positions of UO$_2$ (61). The theoretical models are built from the scattering paths of the photoelectron from the first few shells of atoms surrounding the absorbing atom. The error analysis and the goodness-
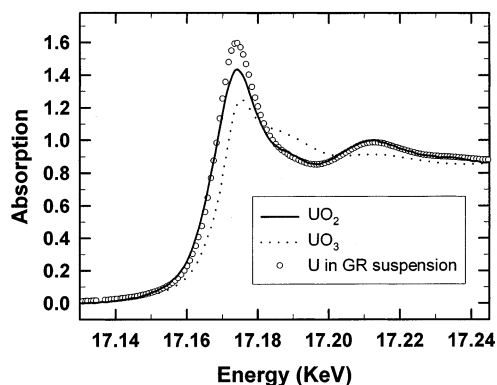
FIGURE 1. Comparison of normalized U L$_{III}$-XANES spectra for UO$_3$, UO$_2$, and uranium in a green rust suspension.

FIGURE 2. Average $\chi(k)^*$ k^2 data for uranium in a green rust suspension.

FIGURE 3. The magnitude of the Fourier transform of $\chi k)^*$ k^2 data (2.5−11.5 Å^{-1} for uranium in a green rust suspension and in UO$_2$.

of-fit parameters were calculated by the fitting routine FEFFIT (62). The structural parameters determined in a fit to the EXAFS data include N_{degen} and R, which are the number of and distance to the neighboring atoms for a single scattering path, respectively, and σ^2, which is the relative mean square displacement of the distance from the absorbing uranium atom to the neighboring atoms for a single scattering path.

XRD Analysis. The XRD analysis of green rust samples was performed using a Rigaku MiniFlex X-ray diffractometer with Ni-filtered Cu Kα radiation. Samples for XRD analysis were prepared by mixing the wet pastes with glycerol to minimize oxidation (63) and smeared on 22-mm-wide glass plates. The samples were scanned from 6 to 80° 2θ at a speed of 1° 2θ min^{-1}. The XRD data were processed using Jade 6.0 (Materials Data, Inc., Livermore, CA).

Transmission Electron Microscopy. Samples for TEM were prepared by resuspending subsamples of the U-GR pastes in deoxygenated distilled water and placing 10−20 μL of these suspensions on Cu TEM grids with holey carbon films. The samples were allowed to air-dry under anoxic conditions for at least 12 h. The samples were stored under anoxic conditions prior to imaging, except for a brief (1−2 s) exposure to air during transfer of the sample holder to the vacuum chamber on the microscope. Specimens were imaged by using a FEI-Philips CM30 TEM operating at 300 kV and a JEOL 4000EXII TEM operating at 400 kV in the Electron Microscopy Collaborative Research Center at Argonne National Laboratory. Dark-field images were formed by using one or more diffracted beams. In a dark-field image, only particles satisfying the specific diffracting condition "light up" in the image; however, for printing purposes the dark-field image contrast has been inverted, and thus the particles in the proper diffracting condition appear as dark patches on a light colored background. High-resolution TEM images were formed by using the unscattered (000) beam and many diffracted beams; the interference of the electron beams gives rise to the lattice fringe patterns.

Results and Discussion

Uranium Reduction and Formation of Nanoparticulate UO$_2$. Uranyl is readily removed from solution in the presence of green rust. Within 48 h, solution-phase uranium concentrations decreased from 4.4 mM to 420 nM, as determined by ICP-OES. The final pH of the suspensions was 6.7. As previously discussed, XANES provides information on the oxidation state of an atom, as indicated by the energy of the adsorption edge. The XANES spectra of UO$_3$ (in the form of γ-UO$_3$), UO$_2$, and U-GR (Figure 1) clearly show that the U^{VI} added to the green rust suspension was reduced to U^{IV}. XRD analysis of the U-GR pastes indicated that the reduction of U^{VI} to U^{IV} is accompanied by the partial oxidation of green rust to magnetite.
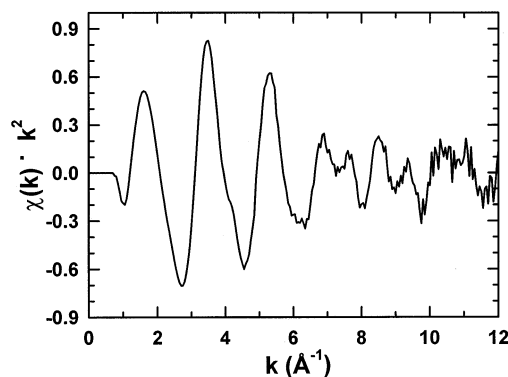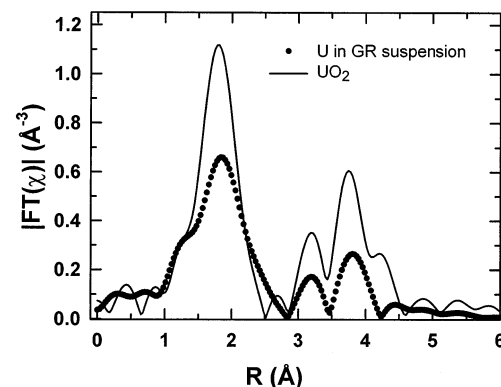
Information on the local environment of uranium atoms in the U-GR samples is provided by analysis of the EXAFS data. The U L$_{III}$-edge background-subtracted, k^2-weighted $\chi(k)$ data from a U-GR sample are shown in Figure 2. A qualitative comparison of the Fourier transformed $\chi(k)^*$ k^2 EXAFS data of UO$_2$ and uranium in the green rust suspension indicates an average local chemical environment about uranium in the green rust sample similar to that of uranium in UO$_2$ (Figure 3). However, the decrease in Fourier transform amplitude of the U-GR sample relative to the UO$_2$ standard indicates a decrease in the average number of atoms surrounding uranium and/or an increase in the disorder of the average local environment of uranium in the U-GR sample. This qualitative observation is consistent with the presence of multiple uranium environments, which can be explained by a combination of one or more of the following scenarios: (1) uranium sorption to the iron oxide surface, (2) the formation of a UO$_2$ precipitate/coating on the iron oxide surface, (3) the formation of UO$_2$ nanoparticles, or (4) self-absorption effects.

A theoretical model based on the crystal structure of UO$_2$ was generated by using FEFF7 (60). The UO$_2$ data were modeled first to determine the important scattering paths of the photoelectron. The data and fit ranges are listed in the caption of Table 1. The paths from the absorbing atom (U) to the first oxygen shell (O1), the first uranium shell (U1), and a second oxygen shell (O2), plus the multiple scattering paths from two oxygen atoms in the first shell (U−O1−O1, U−O1−U−O1$_a$, and U−O1−U−O1$_b$), all contributed significantly to the EXAFS data. These paths, along with their parameterizations, are in Table 2. Including the multiple scattering paths in the model improved the quality of the fit slightly without adding any additional parameters, thus reducing the χ_ν^2-value by 25%. We determined the number of nearest-neighbor uranium atoms in the fit to the UO$_2$ data

TABLE 1. Best-Fit Values for the U-GR and UO$_2$ Sample[c]

path[a]	N_{degen}	R (Å)	σ^2 (10^{-3} Å^2)
U-GR Sample			
U−O1	7.8 ± 0.5	2.34 ± 0.01	13 ± 2
U−U1	5.4 ± 1.1	3.84 ± 0.01	9 ± 2
U−O1−O1	7.8 ± 0.5	4.68 ± 0.02	27 ± 4
U−O1−U−O1$_a$	7.8 ± 0.5	4.68 ± 0.02	27 ± 4
U−O1−U−O1$_b$	7.8 ± 0.5	4.68 ± 0.02	27 ± 4
UO$_2$ Sample			
U−O1	8[b]	2.35 ± 0.01	9 ± 2
U−U1	11.4 ± 4.0	3.87 ± 0.01	5 ± 2
U−O2	22.8 ± 7.9	4.49 ± 0.02	10 ± 3
U−O1−O1	8[b]	4.70 ± 0.03	19 ± 4
U−O1−U−O1$_a$	8[b]	4.70 ± 0.03	19 ± 4
U−O1−U−O1$_b$	8[b]	4.70 ± 0.03	19 ± 4

[a] Single scattering paths are denoted as U−X, where X is the type of atom in a shell about the absorbing U atom (e.g., O1, U1, and O2 for first oxygen shell, the first uranium shell, and a second oxygen shell, respectively). The multiple scattering path U−O1−O1 is from the absorbing U atom to an O1 atom and then to the opposite O1 atom aligned with that U atom and the first O1 atom. The multiple scattering path U−O1−U−O1$_a$ is a focusing path from the absorbing U atom to an O1 atom and then back through the absorbing U atom to the opposite O1 atom aligned with that U atom and the first O1 atom. The multiple scattering path U−O1−U−O1$_b$ is the double scattering path from the absorbing U atom to an O1 atom, back to the U atom, returning to the same O1 atom, and back a second time to the U atom. [b] Uranium in the uraninite structure is 8-fold coordinated by oxygen. [c] S_0^2 was determined from the UO$_2$ data to be 0.9 ± 0.1. ΔE_0 was determined to be 1.9 ± 1.3 and 3.6 ± 0.5 for all paths of the UO$_2$ and U-GR data, respectively. A total of 10 parameters were determined in the fit to 19 independent points in the data, determined from the data range (3.0−11.5 Å^{-1}; 2.5−11.5 Å^{-1}) and fit range (1.0−4.2 Å; 1.0−4.2 Å) for the UO$_2$ and U-GR data, respectively.

TABLE 2. Parameterization for the UO$_2$ Structure[b]

path[a]	N_{degen}	ΔR (Å)	σ^2 (Å^2)
U−O1	N_1	ΔR_1	σ^2_1
U−U1	N_2	ΔR_2	σ^2_2
U−O2	$2 \times N_2$	ΔR_3	σ^2_3
U−O1−O1	N_1	$2 \times \Delta R_1$	$2 \times \sigma^2_1$
U−O1−U−O1$_a$	N_1	$2 \times \Delta R_1$	$2 \times \sigma^2_1$
U−O1−U−O1$_b$	N_1	$2 \times \Delta R_1$	$2 \times \sigma^2_1$

[a] Single scattering paths are denoted as U−X, where X is the type of atom in a shell about the absorbing U atom (e.g., O1, U1, and O2 for first oxygen shell, the first uranium shell, and a second oxygen shell, respectively). The multiple scattering path U−O1−O1 is from the absorbing U atom to an O1 atom and then to the opposite O1 atom aligned with that U atom and the first O1 atom. The multiple scattering path U−O1−U−O1$_a$ is a focusing path from the absorbing U atom to an O1 atom and then back through the absorbing U atom to the opposite O1 atom aligned with that U atom and the first O1 atom. The multiple scattering path U−O1−U−O1$_b$ is the double scattering path from the absorbing U atom to an O1 atom, back to the U atom, returning to the same O1 atom, and back a second time to the U atom. [b] One overall S_0^2 value and one ΔE_0 value were also determined in the fit to the data.

FIGURE 4. The magnitude (a) and the real part (b) of the Fourier transform of the $\chi(k)* k^2$ best-fit model and data from UO$_2$ and U-GR samples.

to illustrate the ability of this model to accurately determine these values. The expected value for the UO$_2$ structure, 12 nearest-neighbor uranium atoms, agrees well with our best-fit value of 11.4 ± 4.0. The fit to the UO$_2$ data is shown in Figure 4, and the best-fit values to these data are listed in Table 1.

The model was applied to the U-GR data as shown in Figure 4; the best-fit values are listed in Table 1. The second oxygen shell (O2) in the U-GR data was found to have a large structural disorder (σ^2) component, indicating that the second oxygen shell is negligible; therefore, this path was removed from the model. The goodness-of-fit parameters for the U-GR ($\mathscr{R}$ = 4%, χ_ν^2 = 20) and UO$_2$ ($\mathscr{R}$ = 2%, χ_ν^2 = 30) data are comparable, indicating that the model is appropriate for both systems. For the U-GR data the best-fit value for the number
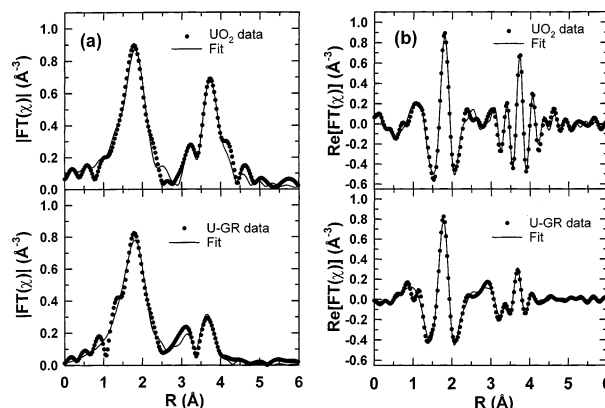
of first-shell oxygen atoms is 7.8 ± 0.5, consistent with U^{IV} and the UO$_2$ structure. However, the number of nearest-neighbor uranium atoms has decreased from 12 for the UO$_2$ structure to 5.4 ± 1.1 for the U-GR sample. These results show that the decrease in the overall amplitude of the XAFS signal for the U-GR data versus the UO$_2$ data is not due to self-absorption effects because fit results from data with self-absorption effects would appear as low coordination numbers for all shells. The decrease in the number of nearest-neighbor uranium atoms in the U-GR system indicates that uranium atoms at the surface of the UO$_2$ phase in the U-GR sample contribute significantly to the average number of near-neighbor uranium atoms in the entire sample. This result is consistent with either a very thin plating of UO$_2$ on the green rust particles or very small particles of UO$_2$. If each uranium atom on the surface of UO$_2$ has four near-neighbor uranium atoms, then the best-fit value for the average number of uranium atoms corresponds to a particle with a diameter of 1.7 ± 0.6 nm.

The formation of discrete nanoparticles of UO$_2$ suggested by the modeling of the EXAFS data was confirmed by TEM imaging (Figure 5). The dark-field image, made by using arcs of the (111) and (200) diffuse rings of the electron diffraction pattern of UO$_2$, clearly shows the formation of discrete particles of UO$_2$, primarily along the edges of the hexagonal green rust crystals. The UO$_2$ particles are typically 2−9 nm in diameter, as determined from the dark-field images and corroborated with the high-resolution images. The size range for the UO$_2$ particles is in agreement with the predicted size range from the EXAFS modeling. The electron diffraction pattern (shown as an inset in Figure 5) shows the hexagonal c-axis spot pattern of a single green rust crystal and the diffuse polycrystalline ring pattern of the nanoparticulate UO$_2$. The d spacings for UO$_2$ measured from the diffraction pattern [(111) 3.23 Å; (200) 2.76 Å; (220) 2.02 Å; (311) 1.67 Å] are in good agreement with published values (64).

Implications for Subsurface Uranium Biogeochemistry and Remediation. The chemical speciation of uranium, particularly its valence state, has a profound effect on the fate of uranium in the subsurface, especially with respect to uranium ore-forming processes and the in situ remediation of uranium-contaminated groundwater. In the last 10 years considerable attention has been focused on the role of microbial processes in the subsurface fate and transport of uranium. Numerous researchers have shown direct enzymatic reduction of U^{VI} species to U^{IV}, primarily UO$_2$, by a phylogenetically diverse array of bacteria (2−4, 65−68, among others), suggesting that these microorganisms play a significant role in the speciation of uranium in the subsurface.
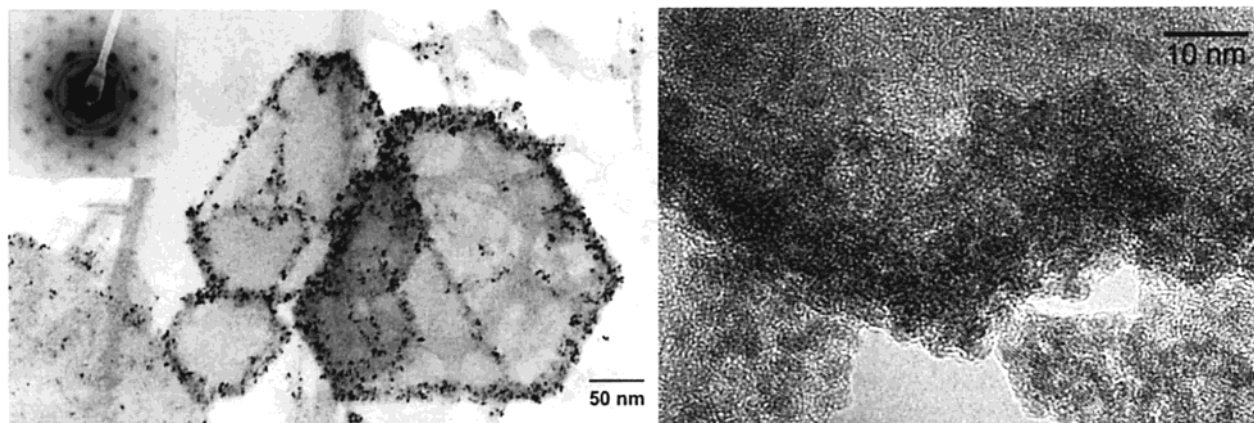
FIGURE 5. TEM images of U-GR particles. The image on the left is a dark-field image of U-GR particles made by using arcs of the (111) and (200) diffuse rings of the electron diffraction pattern of UO_2. (The image contrast was inverted for ease of printing.) The high-resolution image on the right shows highly crystalline UO_2 nanoparticles. The electron diffraction pattern (upper left of left image) shows the hexagonal *c*-axis spot pattern of the single-crystal green rust and the polycrystalline ring pattern of the UO_2. The rings from the UO_2 are somewhat diffuse because of the small size (2−9 nm) of the UO_2 particles.

Indeed, field and laboratory studies indicate that the reduction of U^{VI} to U^{IV} is microbially mediated in many subsurface environments (69−71). However, it is often unclear whether the observed reduction of uranium is due to direct enzymatic reduction or results from interaction of U^{VI} species with reductants resulting from dissimilatory iron or sulfate reduction (i.e., sorbed Fe^{II} and Fe^{II}-bearing minerals as well as reduced sulfur species). Therefore, it is likely that uranium reduction in the subsurface is the result of both direct microbial reduction and coupled biotic-abiotic processes. Indeed, it has been suggested that the reduction of U^{VI} to U^{IV} following the migration of U^{VI} into anoxic zones with a history of DIR activity might be dominated by reaction with biogenic Fe^{II} products, rather than by direct microbial reduction (2). Moreover, the recent identification of green rusts as products of dissimilatory iron reduction, coupled with the ability of green rust to reduce U^{VI}, suggests that green rusts may play an important role in the speciation of uranium in iron-reducing environments. Additional research is needed to better define the conditions that favor the formation of biogenic green rusts in the subsurface; however, stimulating the biogenic formation of green rusts in the subsurface (as well as injection and dispersion of green rust slurries into the subsurface) might prove effective for creating in situ permeable reactive barriers (PRBs) for the remediation of uranium (and other inorganic and organic contaminants).

The reduction of U^{VI} by green rusts is also relevant to the use of zerovalent iron PRBs for the remediation uranium-contaminated groundwater. Laboratory and field studies indicate that zerovalent iron is effective for the removal of U^{VI} from aqueous solutions (72−75); however, the long-term performance of iron metal PRBs is unknown. As mentioned earlier, green rusts have been identified as products of both abiotic and microbially induced corrosion of iron and steel (16−19), and the formation of green rusts in zerovalent iron PRBs has been reported by several investigators (20−23). Although the direct transfer of electrons from zerovalent iron to uranyl is believed to be the dominant mechanism for U^{VI} reduction in iron metal systems, the role of Fe^{II} species has been largely overlooked. Moreover, as the iron metal becomes oxidized (by the reduction of water, U^{VI}, and other oxidants that may be present), layers of corrosion products (including green rust) accumulate on the metal surface, resulting in gradual passification. Under these conditions, the role of Fe^{II} species in the reduction of contaminants (including U^{VI}) in aqueous iron metal systems is likely to be more significant. Thus, the reduction of U^{VI} by green rusts may have implica-

tions for the long-term performance of zerovalent iron PRBs used for the treatment of U^{VI}-contaminated groundwater.

Given the relatively low aqueous solubility of U^{IV} species, the formation of U^{IV}-bearing mineral phases is commonly observed after the biotic or abiotic reduction of U^{VI} (2−4, 13, 69, 76−78). These mineral phases are often fine grained, with particles ranging in size from 10^{-7} to 10^{-9} m. Indeed, the reduction of U^{VI} by *Desulfosporosinus* sp. results in the formation of UO_2 ranging in size from molecular-scale clusters to nanoscale crystals (generally < 3 nm) (68). Our results indicate that nanocrystals of UO_2 can also be formed via the abiotic reduction of U^{VI} by green rust. The formation of nanoparticulate U^{IV} phases might have implications for the transport of U in suboxic environments. Though the reduction of U^{VI} to U^{IV} is generally viewed as an attractive approach for the in situ immobilization/stabilization of U in contaminated groundwater, UO_2 nanoparticles might be relatively mobile in some subsurface environments. Indeed, recent studies indicate the potential for colloid-facilitated transport of radionuclides in the subsurface (79, 80); however, conclusive evidence has been elusive (81). Clearly, additional research is needed to determine the behavior of UO_2 nanoparticles in relevant geological matrices.

Acknowledgments

Literature Cited

(1) Riley, R. G.; Zachara, J. M.; Wobber, F. J. *Chemical contaminants on DOE lands and selection of contaminant mixtures for subsurface science research*; U.S. Department of Energy: 1992.
(2) Fredrickson, J. K.; Zachara, J. M.; Kennedy, D. W.; Duff, M. C.; Gorby, Y. A.; Li, S.-M. W.; Krupka, K. M. *Geochim. Cosmochim. Acta* **2000**, *64*, 3085−3098.

(3) Gorby, Y. A.; Lovley, D. R. *Environ. Sci. Technol.* **1992**, *26*, 205–207.

(4) Lovley, D. R.; Phillips, E. J. P. *Appl. Environ. Microbiol.* **1992**, *58*, 850–856.

(5) Lovley, D. R.; Phillips, E. J. P. *Environ. Sci. Technol.* **1992**, *26*, 2228–2234.

(6) Bell, P. E.; Mills, A. L.; Herman, J. S. *Appl. Environ. Microbiol.* **1987**, *53*, 2610–2616.

(7) Dong, H.; Fredrickson, J. K.; Kennedy, D. W.; Zachara, J. M.; Kukkadapu, R. K.; Onstott, T. C. *Chem. Geol.* **2000**, *169*, 299–318.

(8) Fredrickson, J. K.; Zachara, J. M.; Kennedy, D. W.; Dong, H.; Onstott, T. C.; Hinman, N. W.; Li, S.-M. *Geochim. Cosmochim. Acta* **1998**, *62*, 3239–3257.

(9) Kostka, J. E.; Nealson, K. H. *Environ. Sci. Technol.* **1995**, *29*, 2535–2540.

(10) Kostka, J. E.; Stucki, J. W.; Nealson, K. H.; Wu, J. *Clays Clay Miner.* **1996**, *44*, 522–529.

(11) Galloway, W. E. *Econ. Geol.* **1978**, *73*, 1655–1676.

(12) Posey-Dowty, J.; Axtmann, E.; Crerar, D.; Borcsik, M.; Ronk, A.; Woods, W. *Econ. Geol.* **1987**, *82*, 184–194.

(13) Wersin, P.; Hochella, M. F. J.; Persson, P.; Redden, R.; Leckie, J. O.; Harris, D. *Geochim. Cosmochim. Acta* **1994**, *58*, 2829–2843.

(14) Charlet, L.; Silvester, E.; Liger, E. *Chem. Geol.* **1998**, *151*, 85–93.

(15) Liger, E.; Charlet, L.; Van Cappellen, P. *Geochim. Cosmochim. Acta* **1999**, *63*, 2939–2955.

(16) Bigham, J. M.; Tuovinen, O. H. In *Planetary Ecology*; Caldwell, D. E., Brierley, J. A., Brierley, C. L., Eds.; Van Nostrand Reinhold Co.: New York, 1985; pp 239–250.

(17) Génin, J.-M. R.; Refait, P.; Olowe, A. A.; Abdelmoula, M.; Fall, I.; Drissi, S. H. *Hyp. Int.* **1998**, *112*, 47–50.

(18) Kumar, A. V. R.; Singh, R.; Nigam, R. K. *J. Radioanal. Nuclear Chem.* **1999**, *242*, 131–137.

(19) Refait, P.; Abdelmoula, M.; Génin, J.-M. R. *Corros. Sci.* **1998**, *40*, 1547–1560.

(20) Gu, B.; Phelps, T. J.; Liang, L.; Dickey, M. J.; Roh, Y.; Kinsall, B. L.; Palumbo, A. V.; Jacobs, G. K. *Environ. Sci. Technol.* **1999**, *33*, 2170–2177.

(21) Johnson, T. L.; Tratnyek, P. G. In *In Situ Remediation: Scientific Basis for Current and Future Technologies. Thirty-third Hanford Symposium on Health and the Environment, November 7–11, 1994, Pasco, Washington, USA*; Gee, G. W., Wing, N. R., Eds.; Battelle Press: Columbus, OH, 1994; Vol. 2, pp 931–947.

(22) Roh, Y.; Lee, S. Y.; Elless, M. P. *Environ. Geol.* **2000**, *40*, 184–194.

(23) Vogan, J. L.; Butler, B. J.; Odziemkowski, M. S.; Friday, G.; Gillham, R. W. In *Designing and Applying Treatment Technologies: Remediation of Chlorinated and Recalcitrant Compounds*; Wickramanayake, G. B., Hinchee, R. E., Eds.; Battelle Press: Columbus, OH, 1998; pp 163–168.

(24) Glasauer, S.; Langley, S.; Beveridge, T. J. *Science* **2002**, *295*, 117–119.

(25) Kukkadapu, R. K.; Zachara, J. M.; Smith, S. C.; Fredrickson, J. K.; Liu, C. *Geochim. Cosmochim. Acta* **2001**, *65*, 2913–2924.

(26) Ona-Nguema, G.; Abdelmoula, M.; Jorand, F.; Benali, O.; Géhin, A.; Block, J.-C.; Génin, J.-M. R. *Environ. Sci. Technol.* **2002**, *36*, 16–20.

(27) Parmar, N.; Gorby, Y. A.; Beveridge, T. J.; Ferris, F. G. *Geomicrobiol. J.* **2001**, *18*, 375–385.

(28) Chaudhuri, S. K.; Lack, J. G.; Coates, J. D. *Appl. Environ. Microbiol.* **2001**, *67*, 2844–2848.

(29) Ponnamperuma, F. N.; Tianco, E. M.; Loy, T. *Soil Sci.* **1967**, *103*, 374–382.

(30) Loyaux-Lawniczak, S.; Refait, P.; Ehrhardt, J.-J.; Lecomte, P.; Génin, J.-M. R. *Environ. Sci. Technol.* **2000**, *34*, 438–443.

(31) Olowe, A. A.; Marie, Y.; Refait, P.; Génin, J.-M. R. *Hyp. Int.* **1994**, *93*, 1783–1788.

(32) Perez, O. P.; Umetsu, Y.; Sasaki, H. *Hydrometallurgy* **1998**, *50*, 223–242.

(33) Refait, P.; Génin, J.-M. R. *Corros. Sci.* **1997**, *39*, 539–553.

(34) Schwertmann, U.; Taylor, R. M. In *Minerals in Soil Environments*; Dixon, J. B., Weed, S. B., Eds.; Soil Science Society of America: Madison, WI, 1977; pp 145–180.

(35) Srinivasan, R.; Lin, R.; Spicer, R. L.; Davis, B. H. *Colloids Surfaces A: Physiochem. Eng. Aspects* **1996**, *113*, 97–105.

(36) Lin, R.; Spicer, R. L.; Tungate, F. L.; Davis, B. H. *Colloids Surfaces A: Physiochem. Eng. Aspects* **1996**, *113*, 79–96.

(37) Abdelmoula, M.; Trolard, F.; Bourrié, G.; Génin, J.-M. R. *Hyp. Int.* **1998**, *112*, 235–238.

(38) Trolard, F.; Génin, J.-M. R.; Abdelmoula, M.; Bourrié, G.; Humbert, B.; Herbillon, A. *Geochim. Cosmochim. Acta* **1997**, *61*, 1107–1111.

(39) Génin, J.-M. R.; Bourrié, G.; Trolard, F.; Abdelmoula, M.; Jaffrezic, A.; Refait, P.; Maitre, V.; Humbert, B.; Herbillon, A. *Environ. Sci. Technol.* **1998**, *32*, 1058–1068.

(40) Bourrié, G.; Trolard, F.; Génin, J.-M. R.; Jaffrezic, A.; Maître, V.; Abdelmoula, M. *Geochim. Cosmochim. Acta* **1999**, *63*, 3417–3427.

(41) Erbs, M.; Hansen, H. C. B.; Olsen, C. E. *Environ. Sci. Technol.* **1999**, *33*, 307–311.

(42) O'Loughlin, E. J.; Burris, D. R. Reductive transformation of halogenated hydrocarbons by green rust. *220th American Chemical Society National Meeting* **2000**, *40*(2) 635–637.

(43) Williams, A. G. B.; Scherer, M. M. *Environ. Sci. Technol.* **2001**, *35*, 3488–3494.

(44) Myneni, S. C. B.; Tokunaga, T. K.; Brown, G. E., Jr. *Science* **1997**, *278*, 1106–1109.

(45) Refait, P.; Simon, L.; Génin, J.-M. R. *Environ. Sci. Technol.* **2000**, *34*, 819–825.

(46) Hansen, H. C. B.; Borggaard, O. K.; Sorensen, J. *Geochim. Cosmochim. Acta* **1994**, *58*, 2599–2608.

(47) Hansen, H. C. B.; Guldberg, S.; Erbs, M.; Bender Koch, C. *Appl. Clay Sci.* **2001**, *18*, 81–91.

(48) Tamaura, Y. *Inorg. Chem.* **1985**, *24*, 4363–4366.

(49) Refait, P.; Abdelmoula, M.; Trolard, F.; Génin, J.-M. R.; Ehrhardt, J. J.; Bourrié, G. *Am. Mineral.* **2001**, *86*, 731–739.

(50) Refait, P.; Drissi, H.; Marie, Y.; Génin, J.-M. R. *Hyp. Int.* **1994**, *90*, 389–394.

(51) Roh, Y.; Lee, S. Y.; Elless, M. P.; Foss, J. E. *Clays Clay Miner.* **2000**, *48*, 266–271.

(52) Koningsberger, D. C.; Prins, R., Eds. *X-ray Absorption: Principles, Applications, Techniques of EXAFS, SEXAFS and XANES*; John Wiley and Sons: New York, 1988; Vol. 92.

(53) Durham, P. J. In *X-ray Absorption: Principles, Applications, Techniques of EXAFS, SEXAFS and XANES*; Koningsberger, D. C., Prins, R., Eds.; John Wiley and Sons: New York, 1988; Vol. 92, pp 53–84.

(54) Stern, E. A. In *X-ray Absorption: Principles, Applications, Techniques of EXAFS, SEXAFS and XANES*; Koningsberger, D. C., Prins, R., Eds.; John Wiley and Sons: New York, 1988; Vol. 92, pp 3–51.

(55) Segre, C. U.; Leyarovska, N. E.; Chapman, L. D.; Lavender, W. M.; Plag, P. W.; King, A. S.; Kropf, A. J.; Bunker, B. A.; Kemner, K. M.; Dutta, P.; Duran, R. S.; Kaduk, J. In *Synchrotron Radiation Instrumentation: Eleventh U.S. National Conference*; Pianetta, P. A., Arthur, J. R., Brennan, S., Eds.; American Institute of Physics: New York, 2000; Vol. CP5321, pp 419–422.

(56) Stern, E. A.; Heald, S. M. *Rev. Sci. Instrum.* **1979**, *50*, 1579–1583.

(57) Kemner, K. M.; Kropf, J.; Bunker, B. A. *Rev. Sci. Instrum.* **1994**, *65*, 3667–3669.

(58) Cross, J. L.; Frenkel, A. I. *Rev. Sci. Instrum.* **1998**, *70*, 38–40.

(59) Stern, E. A.; Newville, M.; Ravel, B.; Yacoby, Y.; Haskel, D. *Physica B* **1995**, *208/209*, 117–120.

(60) Zabinsky, S. I.; Rehr, J. J.; Ankudinov, A.; Albers, R. C.; Eller, M. J. *Phys. Rev. B* **1995**, *52*, 2995–3009.

(61) Wyckoff, R. W. G. *Crystal Structures*; Interscience Publishers: New York, 1960.

(62) Newville, M.; Ravel, B.; Haskel, D.; Stern, E. A. *Physica B* **1995**, *208/209*, 154–156.

(63) Hansen, H. C. B.; Koch, C. B. *Clay Miner.* **1998**, *33*, 87–101.

(64) Rundle, R. E.; Baenziger, N. C.; Wilson, A. S.; McDonald, R. A. *J. Am. Chem. Soc.* **1948**, *70*.

(65) Francis, A. J.; Dodge, C. J.; Lu, F.; Halada, G. P.; Clayton, C. R. *Environ. Sci. Technol.* **1994**, *28*, 636–639.

(66) Fredrickson, J. K.; Kostandarithes, H. M.; Li, S. W.; Plymale, A. E.; Daly, M. J. *Appl. Environ. Microbiol.* **2000**, *66*, 2006–2011.

(67) Kashefi, K.; Lovley, D. R. *Appl. Environ. Microbiol.* **2000**, *66*, 1050–1056.

(68) Suzuki, Y.; Kelly, S. D.; Kemner, K. M.; Banfield, J. F. *Nature* **2002**, *419*, 134.

(69) Abdelouas, A.; Lutze, W.; Gong, W.; Nuttall, E. H.; Strietelmeier, B. A.; Travis, B. J. *Sci. Tot. Environ.* **2000**, *250*, 21–35.

(70) Barnes, C. E.; Cochran, J. K. *Geochim. Cosmochim. Acta* **1993**, *57*, 555–569.

(71) Senko, J. M.; Istok, J. D.; Suflita, J. M.; Krumholz, L. R. *Environ. Sci. Technol.* **2002**, *36*, 1491–1496.

(72) Farrell, J.; Bostick, W. D.; Jarabeck, R. J.; Fiedor, J. N. *Ground Water* **1999**, *37*, 618–624.

(73) Fiedor, J. N.; Bostick, W. D.; Jarabek, R. J.; Farrell, J. *Environ. Sci. Technol.* **1998**, *32*, 1466−1472.

(74) Gu, B.; Liang, L.; Dickey, M. J.; Yin, X.; Dai, S. *Environ. Sci. Technol.* **1998**, *32*, 3366−3373.

(75) Morrison, S. J.; Metzler, D. R.; Carpenter, C. E. *Environ. Sci. Technol.* **2001**, *35*, 385−390.

(76) Abdelouas, A.; Lu, Y.; Lutze, W.; Nuttall, H. E. *J. Contam. Hydrol.* **1998**, *35*, 217−233.

(77) Abdelouas, A.; Lutze, W.; Nuttall, H. E. *J. Contam. Hydrol.* **1999**, *36*, 353−375.

(78) Ho, C. H.; Miller, N. H. *J. Colloid Interface Sci.* **1986**, *113*, 232−240.

(79) Kaplan, D. I.; Bertsch, P. M.; Adriano, D. C.; Orlandini, K. A. *Radiochim. Acta* **1994**, *66/67*, 181−187.

(80) Kersting, A. B.; Efurd, D. W.; Finnegan, D. L.; Rokop, D. J.; Smith, D. K.; THompson, J. L. *Nature* **1999**, *397*, 56−59.

(81) Marty, R. C.; Bennett, D.; Thullen, P. *Environ. Sci. Technol.* **1997**, *31*, 2020−2027.